

Journal of Materials Chemistry A

Accepted Manuscript



This is an *Accepted Manuscript*, which has been through the Royal Society of Chemistry peer review process and has been accepted for publication.

Accepted Manuscripts are published online shortly after acceptance, before technical editing, formatting and proof reading. Using this free service, authors can make their results available to the community, in citable form, before we publish the edited article. We will replace this *Accepted Manuscript* with the edited and formatted *Advance Article* as soon as it is available.

You can find more information about *Accepted Manuscripts* in the [Information for Authors](#).

Please note that technical editing may introduce minor changes to the text and/or graphics, which may alter content. The journal's standard [Terms & Conditions](#) and the [Ethical guidelines](#) still apply. In no event shall the Royal Society of Chemistry be held responsible for any errors or omissions in this *Accepted Manuscript* or any consequences arising from the use of any information it contains.



Journal Name

ARTICLE

Anti-aggregation and intra-type Förster resonance energy transfer in bulky size indoline sensitizer for dye-sensitized solar cells: A combined DFT/TDDFT and molecular dynamics study

Wei-Lu Ding, Quan-Song Li* and Ze-Sheng Li*

2Received 00th January 20xx,
Accepted 00th January 20xx

DOI: 10.1039/x0xx00000x

www.rsc.org/

We have performed theoretical investigation by combination of DFT/TDDFT and molecular dynamics simulation to explain the relationship between the bulky size donor group and higher efficiency for a recent indoline sensitizer YA422 derived from its counterparts IQ4 and YA421, which featured the gradual extended donor subunit in dye-sensitizer solar cells (DSSCs). Firstly, the absorption and fluorescence properties indicate that the Förster resonance energy transfer occurs only in YA422, where the λ_{ems} of donor group D2 matches with the λ_{abs} in whole molecule around the band of 533 nm. Second, the simulated heterogeneous between the sensitizer and (TiO₂)₁₂₄ before and after the additive CDCA co-adsorption shows that the nearest position of every monomer in YA422 is separated by a row of Ti atoms due to its steric hindrance introduced by the extended donor group, which not only forms the ordered alignment but also prevents aggregation. Meanwhile, the separated position decreases the self-decay which indicated by the complete intramolecular charge transfer in the aggregate structure on (TiO₂)₁₂₄. Furthermore, by combined Newns-Anderson approach and Marcus equation, the faster electron injection rate k_{inject} of YA422 ($2.27 \times 10^{15} \text{ s}^{-1}$) is obtained compared with IQ4 and YA421. We confirm that the higher conversion efficiency achieved by YA422 is aroused from its bulky size donor group which enhances the electron-donating and transfer. Finally, based on the above insights, we designed a novel sensitizer DW1 which is expected to be promising candidate due to its enhanced absorption and larger k_{inject} compared with YA422.

1. Introduction

Dye sensitized-solar cells have aroused great interest in academia and engineers in the near decades at the urgent of searching for sustainable and clean energy resources all over the world upon the first report by the pioneer group.¹ Since then, considerable efforts have been made to further improve the conversion efficiency by optimization the components such as sensitizer,²⁻⁸ electrolyte,⁹⁻¹¹ photoanode¹²⁻¹⁴ and counter electrode.^{15, 16} Meanwhile, the most critical mechanisms involved in the photoinduced electron injection and recombination are still kept a high attention because the deeper understanding of the process of electron transfer can guide to synthesis potential candidates before the real device assembly.

In the latter years efforts, however, the conversion efficiencies have not improved obviously, especially in the pure organic sensitizer-based devices because the π - π stacking in its own solution¹⁷ and on the semiconductor surface (commonly

TiO₂)¹⁸ can lead to the fast fluorescence decay from excited state to ground state, and deteriorates the electron injection efficiency.¹⁹⁻²¹ Thus experimental works have focused on co-sensitization via more than one kind of sensitizer²²⁻²⁷ to complement absorption each other^{28, 29} which not only covers the panchromatic window extraordinarily but also produces an outperformance short-circuit density J_{sc} , or co-adsorption with an anti-aggregate additive (commonly the chenodeoxycholic acid (CDCA))^{30, 31} aims to separate the sensitizers one by one and achieves a higher open-circuit voltage V_{oc} .

For the process of co-sensitization, the inter-type Förster resonance energy transfer (FRET)³²⁻³⁸ from the energy donor to acceptor (the former features a shorter-wavelength absorption and coded as “blue” or energy relay dye, while the latter possesses a longer-wavelength response and named as “red” dye) occurs through nonradiative dipole-dipole coupling. This strategy not only decreases the usage of every kind of sensitizer but also improves the overall efficiencies at the compatible ratio.^{29, 34, 39, 40} However, an observation of the detrimental inter-type FRET via experiment⁴¹ says that the weaker dipole-dipole coupling which featured with the relative vertical orientation can enhance the electron injection in “blue dye”, while the more parallel orientation strengthens the intermolecular FRET at the expense of degradation its electron injection. Alternatively, this inter-type FRET can be transferred to intra-type FRET^{38, 42, 43} by end-capping energy donor in energy acceptor directly, as similar as to the “antenna” where

Beijing Key Laboratory of Photoelectric/Electrophotonic Conversion Materials, Key Laboratory of Cluster Science of Ministry of Education, School of Chemistry, Beijing Key Laboratory for Chemical Power Source and Green Catalysis, School of Chemistry, Beijing Institute of Technology, Beijing 100081, China
E-mail: liquansong@bit.edu.cn; zeshengli@bit.edu.cn; Tel: +86 01 6891 8670
Electronic Supplementary Information (ESI) available: See DOI: 10.1039/x0xx00000x

the energy can be transferred without lessening the injection efficiency of the energy donor and this can be embraced.

The representative case is YA422 (Fig. 1),⁴⁴ an indoline sensitizer derivatived from IQ4^{44, 54} and YA421⁴⁴ (Fig. 1), achieves the excellent conversion efficiency of $\eta=10.65\%$ among indoline sensitizer-based devices.⁴⁵⁻⁵³ It has shown that the conversion efficiency is enhanced by the order of IQ4, YA421 and YA422 from 7.57% to 8.84% and then to 9.60% in the $[\text{Co}(\text{bpy})_3]^{2+/3+}$ redox, and finally, a further improvement of 10.65% sensitized by YA422 is obtained by using the gold-doped graphene as the counter electrode.⁴⁴ Although the enhanced conversion efficiency of YA422 is benefitted from the extended donor group which can prevent the $[\text{Co}(\text{bpy})_3]^{2+/3+}$ redox close to TiO_2 surface, the points of view from structure-property, photoinduced energy transfer and electron injection rate are still need to be comprehension deeply.

Therefore, it is the aim of this paper to explore the relationship between the extended donor part and the final efficiency from the sides of the intra-type FRET, the capacity of anti-aggregation and the electron injection rate, respectively. Additionally, the co-adsorption along with the chenodeoxycholic acid (CDCA) is also considered based on experiment to explain whether it is necessary in the bulky size YA421 and YA422.

This paper is organized as follows: methodology introduces the theoretical approach and the model on which the simulations are based. And then the results and discussions analyze 1) the intra-type Förster resonance energy transfer in our defined donor groups (D1(D1')/D2(D2')), Fig. 1) in YA421/YA422, respectively 2) the influence of the extended donor group on the adsorption mode and the role of CDCA on the anti-aggregation in the YA421 and YA422 as well as 3) the electron injection rate of these three sensitizers and 4) the properties of a newly designed sensitizer DW1 (Fig. 1). Final section concludes with a summary.

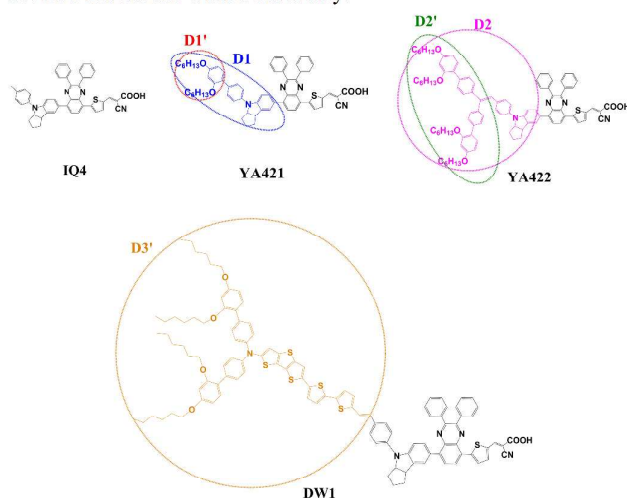


Fig. 1 Molecular structures of IQ4, YA421, YA422 and newly designed candidate DW1. (The D1/D1' in blue/red, the D2/D2' in pink /green and D3' in orange represent the different definition on extended donor subunits in the analysis of Förster resonance energy transfer)

2. Methodology

2.1 Electronic structure computations

For the optimization of isolated sensitizers in ground and oxidized states, the density functional theory (DFT) B3LYP⁵⁵ functional with 6-31G(d)⁵⁶/LANL2DZ⁵⁷ basis set for C, H, O, N, S/Ti atoms were used. The subsequent simulation of frequency based on the optimized geometries was carried out to determine these geometries being indeed the minima on the potential energy surface. For the intermolecular interaction of the dimeric structure on TiO_2 substrate before and after the CDCA co-adsorption, the B3LYP-D3⁵⁸ method was utilized as cut by the substrate. It is known that the calculated vertical excitation energies of different types of molecules depend on the employed functionals. Test calculations have been carried out for IQ4 with several usually employed functionals including BHandHLYP, CAM-B3LYP, PBE0, and MPW1K, where MPW1K shows the best performance with a discrepancy of 0.01 eV with respect to the experiment data (see Table S1 in Electronic Supplementary Information (ESI)). Thus, the optical properties of isolated and dimeric dyes are studied by time-dependent DFT (TDDFT)-MPW1K/6-31+G(d) method in dichloromethane solvent (modeled by C-PCM⁵⁹).

To explain the intra-type Förster resonance energy transfer, the geometric optimization of D1(D1')/D2(D2') subunits in their excited state (S_1) was carried out in CH_2Cl_2 solution by the MPW1K/6-31+G(d) method and the maximum emission λ_{cms} from S_1 to S_0 was then performed because the λ_{cms} is most important in the process of FRET and the emission spectra could not be obtained because frequencies of excited state are not available. All the above mentioned calculations were performed using the Gaussian 09 program of D.01 version.⁶⁰

To model the heterogeneous interfacial of sensitizer and CDCA adsorbed on the anatase TiO_2 (101) surface, a neutral, stoichiometric $(\text{TiO}_2)_{124}$ cluster was selected. For the aggregate pattern, the nomenclature has illustrated in Fig. 2, the first monomer located in (0, 0) position is fixed and another one is labeled by (x, y) coordinates. For aggregate structures of IQ4/YA421/YA422, the most interaction positions of (-1, 1), (1, 1), (-3, 1), (3, 1)/ (1, 1), (0, 2), (2, 2)/ (0, 2), (2, 2) were chosen due to the steric hindrance introduced by the extended donor group. After the optimization of heterogeneous interfacial, molecular dynamics simulation for a total time span of 10 ps was performed to detect the instantaneous variation of distances, such as H-bond and $\text{N}\cdots\text{N}$ atoms which both located on the donor groups. The above mentioned static optimization and dynamic simulation were carried out by the DFTB+ program package^{61, 62} which has shown the adequate accuracy at low computational cost in this field.⁶³⁻⁶⁶

2.2 Analysis of intramolecular Förster resonance energy transfer

To qualitatively discuss the intra-type Förster resonance energy transfer (FRET) between the energy donor and acceptor, we

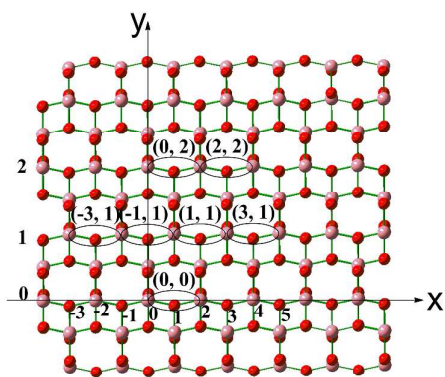


Fig. 2 The aggregate patterns on the $(\text{TiO}_2)_{124}$ cluster.

calculated the orientation factor κ^2 and the position vectors $|r_D - r_A|$, and the FRET rate is expressed as:⁶⁷

$$k_F = \frac{1}{\tau_0} \left(\frac{R_0^6}{|r_A - r_D|^6} \right) \quad (1)$$

where τ_0 is the lifetime of excited state for energy donor, R_0 is the Förster radius when the FRET has 50% probability, and r_D and r_A are the position vectors of energy donor and acceptor respectively. R_0 can be obtained by the luminescence efficiency Q_D of energy donor, the overlap integral of the donor emission spectrum F_D and the acceptor absorption spectrum ε_A along with the orientation factor κ^2 of the dipole-dipole coupling:^{32, 67}

$$R_0^6 = \frac{9000 \times \ln(10) \kappa^2 Q_D}{128 \pi^5 n^4 N_A} \int F_D(\lambda) \varepsilon_A(\lambda) \lambda^4 d\lambda \quad (2)$$

where N_A and n are the Avogadro's constant and the refractive index of the medium, respectively. Notably, the κ^2 can vary from 0 to 4 ($\kappa^2 = 0, 1, 4$ upon the transition dipole moment of energy donor and acceptor is vertical, parallel and end to end, respectively, and $\kappa^2 = 2/3$ of the random orientation⁶⁸) and it is expressed as:⁴¹

$$\kappa^2 = (\sin \alpha_D \sin \alpha_A \cos \beta_{DA} - 2 \cos \alpha_D \cos \alpha_A)^2 \quad (3)$$

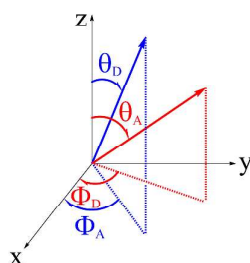
Accordingly, the angles of the two dipoles are related to:⁴¹

$$\alpha_D = \arccos(\sin \theta_D \sin \phi_D) \quad (4)$$

$$\alpha_A = \arccos(\sin \theta_A \sin \phi_A)$$

$$\beta_{DA} = \arctan(\tan \theta_D \cos \phi_D) - \arctan(\tan \theta_A \cos \phi_A)$$

where the angles θ_D, θ_A are defined in the following chart:



2.3 Analysis of interfacial electronic coupling

To obtain a relatively accurate electron-transfer time, Newns-Anderson approach⁶⁹ was employed to compute the mixing of lowest unoccupied molecular orbital (LUMO) on sensitizer with the manifold virtue orbitals on TiO_2 . Accordingly, this mixing possesses a Lorentzian distribution:⁷⁰

$$\rho_{\text{LUMO}}(E) = \frac{1}{(E - E_{\text{LUMO(ads)}})^2 + (\frac{\hbar\Gamma}{2})^2} \quad (5)$$

The broadening width $\hbar\Gamma$ in eqn (5) is taken as the mean deviation of the LUMO (sensitizer) levels, and is defined as follows:⁷¹

$$\hbar\Gamma = \sum_i P_i |\varepsilon_i - E_{\text{LUMO(ads)}}| \quad (6)$$

where $E_{\text{LUMO(ads)}}$ is obtained by a weighted average:⁷¹

$$E_{\text{LUMO(ads)}} = \sum_i P_i \varepsilon_i \quad (7)$$

where P_i and ε_i are the portion of i th molecular orbital (MO) for sensitizer and its corresponding MO energy, respectively. Simultaneously, the P_i is evaluated by:⁷¹

$$P_i = \frac{\sum_{j \in \text{scn}} (c_{ij}^A)^2}{\sum_{j \in \text{scn@TiO}_2} (c_{ij}^A)^2} \quad (8)$$

And then, the heterogeneous electron-transfer time is calculated by the following formula:⁷²

$$\tau(\text{fs}) = \frac{658}{\hbar\Gamma(\text{meV})} \quad (9)$$

2.4 Estimation of electron injection rate

For the aim of comprehension the fast electron injection, the common Marcus eqn (10) of the following form:

$$k_{\text{inject}} = \left(\frac{\pi}{\hbar^2 \chi k_B T} \right)^{1/2} |V_{\text{RP}}|^2 e^{[-(\Delta G_{\text{inject}} + \chi)^2 / 4 \chi k_B T]} \quad (10)$$

is replaced by the eqn (11) with a square root function because the high numerical sensitivity of the exponential function:⁷³

$$k_{\text{inject}} = \left(\frac{\pi}{\hbar^2 \chi k_B T} \right)^{1/2} |V_{\text{RP}}| [-\Delta G_{\text{inject}} - (E_C - E_F - \chi)]^{1/2} \quad (11)$$

where in eqn (11), the χ is the inner reorganization energy which contains the solute part χ^{scn} and the solvent part χ^{sol} :

$$\chi = \chi^{\text{scn}} + \chi^{\text{sol}} = \frac{\chi_1^{\text{scn}} + \chi_2^{\text{scn}}}{2} + \chi^{\text{sol}} \quad (12)$$

Accordingly, the χ^{scn} can be defined as:

$$\chi_1^{\text{scn}} = E_{(Q_r)}^{\text{DBA}^*} - E_{(Q_r)}^{\text{DBA}^*} \quad (13)$$

$$\chi_2^{\text{scn}} = E_{(Q_r)}^{\text{DBA}^+} - E_{(Q_r)}^{\text{DBA}^+} \quad (14)$$

where the $E_{(Q_r)}^{\text{DBA}^*}$, $E_{(Q_r)}^{\text{DBA}^+}$, $E_{(Q_p)}^{\text{DBA}^*}$ and $E_{(Q_p)}^{\text{DBA}^+}$ contribute to the energies obtained from the excited state at the form of cation, energies of the

relaxed excited state, the cationic energies calculated at the geometry of the excited state and the energies of the relaxed cationic state, respectively.

As for the content related to χ^{sol} , it is expressed by:

$$\chi^{\text{sol}} = \Delta q \left(\frac{1}{2R_D} + \frac{1}{2R_A} - \frac{1}{R} \right) \left(\frac{1}{\epsilon_\infty} - \frac{1}{\epsilon_s} \right) \quad (15)$$

where R_D , R_A , R denote the radii of the donor, acceptor and the distances between their centers, and the ϵ_∞ as well as the ϵ_s stand for the optical frequency and static relative dielectric constants of the solvent, respectively. And Δq is the amount of the transferred electron.

Additionally, the coupling constant V_{RP} is estimated via the Generalized Mulliken-Hush formalism (GMH):⁷³

$$|V_{\text{RP}}| = \frac{\mu_{\text{RP}} |\Delta E_{\text{RP}}|}{[(\mu_{\text{R}} - \mu_{\text{P}})^2 + 4\mu_{\text{RP}}^2]^{1/2}} \quad (16)$$

where μ_{RP} and μ_{R} (μ_{P}) stand for the transition dipole moment, the permanent dipole of the excited and cationic state, respectively. In eqn (16), ΔE_{RP} is calculated by:

$$\Delta E_{\text{RP}} = E_{\text{P}} - E_{\text{R}} + E_{\text{CB}}^{\text{SC}} = E_{(\text{Q}_\text{P})}^{\text{DBA}^+} - E_{(\text{Q}_\text{R})}^{\text{DBA}^*} + E_{\text{CB}}^{\text{SC}} \quad (17)$$

In eqn (17), the E_{P} and E_{R} contribute to the energies of the product (cationic state) and the reactant (excited state), respectively.

Furthermore, to compute the electron injection driving force ΔG_{inject} in eqn (11), we assume that the process occurs in relaxation path, thus the ΔG_{inject} can be calculated by:

$$\Delta G_{\text{inject}}^{\text{sen}^*} = E_{\text{ox-relax}}^{\text{sen}^*} - E_{\text{CB}}^{\text{SC}} \quad (18)$$

where the $E_{\text{ox-relax}}^{\text{sen}^*}$ is the excited state oxidation, and it can be expressed as:

$$E_{\text{ox-relax}}^{\text{sen}^*} = E_{\text{ox}}^{\text{sen}} - E_{0-0}^{\text{sen}} \quad (19)$$

In eqn (19), the $E_{\text{ox-relax}}^{\text{sen}}$ and E_{0-0}^{sen} present for the ground state oxidation and the "0-0" absorption energy, respectively, and the latter one can be written as:

$$E_{0-0}^{\text{sen}} = \lambda_{\text{max}} - E_{\text{S}_i}^{\text{reorg}} \quad (20)$$

$$E_{\text{S}_i}^{\text{reorg}} = E_{\text{S}_i}(\text{Q}_{\text{S}_0}) - E_{\text{S}_i}(\text{Q}_{\text{S}_i}) \quad (21)$$

$$E_{\text{S}_i}(\text{Q}_{\text{S}_0}) = E_{\text{S}_0}(\text{Q}_{\text{S}_0}) + \Delta E_{\text{S}_i} \quad (22)$$

where $E_{\text{S}_i}(\text{Q}_{\text{S}_0})$, $E_{\text{S}_i}(\text{Q}_{\text{S}_i})$ and $E_{\text{S}_0}(\text{Q}_{\text{S}_0})$ contribute to the energies for excited state S_i at the ground state S_0 , the energies obtained from the optimized excited state S_i and the energies in the ground state S_0 , respectively. Additionally, the ΔE_{S_i} is the excitation energy from $\text{S}_0 \rightarrow \text{S}_i$.

For analysis of the electron injection rate, we only use the data obtained from eqn (11) unless otherwise noted. And we only provide outline of the classical Marcus theory and the detail is given by ref.73.

3. Results and discussions

3.1 Intra-type Förster resonance energy transfer

As we know, the prerequisite for the high efficiency sensitizer is the absorption can match with the solar radiation in the panchromatic range. Inspired by the more prominent conversion efficiency of YA421 and YA422 compared with IQ4, the optical property of these isolated sensitizers in CH_2Cl_2 solution has been simulated to explore the critical role of the extended donor part D1(D1') and D2/(D2') (Fig. 1) in YA421 and YA422, respectively. The simulated spectra, transition characterization and the oscillator strength f are summarized in Fig. 3 (a) and Table 1, respectively. From Fig. 3 (a), one can find that the maximum absorption λ_{abs} among these sensitizers are all around 530 nm and the oscillator strength f related to this band is improved by the order of YA422 (1.26) > YA421 (1.16) > IQ4 (1.11), respectively. However, in the region of 350-420 nm, the peak is in the order of YA422 (367 nm), IQ4 (405 nm) and YA421 (407 nm), respectively. These results are perfectly in line with the observation by experiment⁴⁴ and imply that the extended donor moiety can improve the absorption strength in the lower energies region and influence the higher energies band apparently.

Table 1 Electronic transition data obtained at MPW1K/6-31+G(d) level for isolated sensitizer in the CH_2Cl_2 solution.

Sensitizer	$\lambda_{\text{abs}}/(\text{nm}/\text{eV})$	$\lambda_{\text{abs}}(\text{exp})^{\text{a}}$	transition character ^b	f
IQ4	529/2.34	526	H→L	1.11
	405/3.06	423	H-1→L	0.61
	302/4.11	/	H→L+3	0.58
YA421	533/2.33	522	H→L	1.16
	407/3.04	413	H-2→L	0.59
	315/3.93	/	H→L+3	0.98
YA422	533/2.32	534	H→L	1.26
	411/3.02	/	H-3→L	0.45
	367/3.38	388	H→L+2	1.53

^a Data from ref.44.

^b H presents for HOMO and L presents for LUMO.

In view of the enhanced absorption strength around the band of 530 nm and the prominent J_{sc} of YA421 and YA422-based device, the intra-type FRET from the extended donor group to energy acceptor has been explored. Initially, the absorption and fluorescence ($\text{S}_1 \rightarrow \text{S}_0$) properties are simulated to detect whether the fluorescence and absorption in energy donor and acceptor are matched in YA421 and YA422, respectively. We assume the two different energy transfer paths in the two sensitizers: the first one is the energy transfer is initially triggered from the D1'/D2' segment (in red and green, Fig. 1) and the second one is supposed from the D1/D2 (in blue and pink, Fig. 1). The absorption λ_{abs} and fluorescence λ_{ems} of $\text{S}_1 \rightarrow \text{S}_0$ in these defined donor parts have been simulated and the corresponding data is summarized in Table 2 and Fig. 3 (b)-(e), respectively. From Table 2, one can find that the λ_{abs} of D1/D1' is around 310/235 nm and the λ_{ems} is around 349/288 nm, respectively. Via the comparison of spectra in Fig. 3 (b), the λ_{abs} of 235 nm in D1'

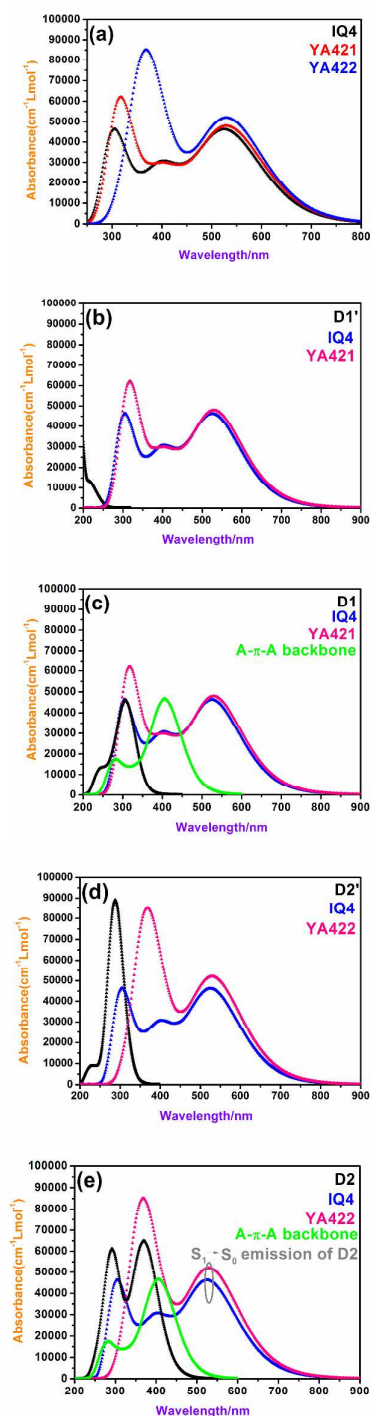


Fig. 3 Simulated absorption spectra in dichloromethane solution (a) for isolated IQ4, YA421 and YA422 (b) for IQ4, YA421 and D1' (c) for IQ4, YA421 and D1 (d) for IQ4, YA422 and D2' (e) for IQ4, YA422 and D2, respectively.

does not involve in the absorption in YA421, and the λ_{ems} of 288 nm in D1' does not match with the λ_{abs} in YA421. While in Fig. 3 (c), the λ_{abs} of 310 nm in D1 and the absorption of 300-400 nm in A- π -A backbone are consisted of the absorption in YA421. Although the absorption band around 310 nm of D1

involves the higher energies excitation of YA421, the λ_{ems} around 349 nm in D1 does not contribute to the energy transfer because the f_{abs} of YA421 in this region is not enhanced, namely, the f_{ems} (1.08) of D1 is stronger than that of the f_{abs} (0.98) related to the band of 315 nm in YA421. Thus, it is speculated that the intra-type FRET does not occur in YA421 based on above analysis. As similar as to the absorption of D1', the λ_{abs} of 292 nm in D2' also does not involve the absorption of YA422 (Fig. 3 (d)), and the λ_{ems} of 348 nm in D2' is not compatible with the absorption of 367 nm in YA422. While for D2, the λ_{abs} of 370 nm is overlapped with the band of 367 nm in YA422, and the absorption of 300-450 nm in A- π -A backbone is also consistent with the absorption of 350-450 nm in YA422 (Fig. 3 (e)). Furthermore, the λ_{ems} of D2 around 533 nm matches well with the absorption of 533 nm in YA422 where the f_{abs} (1.26) in YA422 of this band is enhanced obviously with respect to the f_{ems} (0.93) of this band in D2. Thus, the intra-type FRET might occur only in YA422 that is contributed from D2 segment.

Based on eqn (1)-(4), the position vector $|r_{\text{D}}-r_{\text{A}}|$ and the orientation factor κ^2 between energy donor and acceptor for isolated YA421 and YA422 are 4.52 Å and 5.28 Å, 0.70 and 0.63, respectively. Since smaller $|r_{\text{D}}-r_{\text{A}}|$ and larger κ^2 indicate faster FRET, it seems the FRET capability of YA422 is weaker than that of YA421. Note that most sensitizers in DSSCs are adsorbed on TiO₂ rather than in solution, we further examined these two factors for sensitizers@TiO₂ during a 10 ps dynamics simulation. As shown in Fig.4, YA422 is characterized by smaller $|r_{\text{D}}-r_{\text{A}}|$ and larger κ^2 than that of YA421. This highlights the importance of environment effects and coincides with the optical clues.

Table 2 Spectroscopic parameters for D1(D1') and D2(D2') subunits.

Donor part	$\lambda_{\text{abs}}/\text{nm}$	f_{abs}	$\lambda_{\text{ems}}(\text{S}_1 \rightarrow \text{S}_0)/\text{nm}$	f_{ems}
D1	310	1.05	349	1.08
D1'	235	0.12	288	0.11
D2	370	1.59	533	0.93
D2'	292	0.57	348	1.19

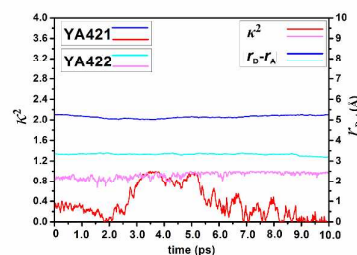


Fig.4 Evolution of position vector $|r_{\text{D}}-r_{\text{A}}|$ and the orientation factor κ^2 for YA421 and YA422 adsorbed on TiO₂ surface.

3.2 Influence of extended donor on the adsorption mode

In general, the sensitizer with a co-planar backbone is inclined to aggregate on TiO₂ substrate and this aggregation contributes to a disordered alignment whereas can be hindered via co-

adsorbent additive chenodeoxycholic acid (CDCA).⁴⁸ Thus, these sensitizers adsorbed on TiO₂ substrate have been simulated before and after the CDCA co-adsorption to explore the relationship between the bulky size donor group and the capacity of anti-aggregation. According to experiment,⁷⁴⁻⁷⁶ the adsorption mode of sensitizer on TiO₂ anatase (101) surface is commonly found three patterns: the monodentate, bidentate chelating and bidentate bridging⁷⁷⁻⁷⁹ and the latter one has been shown more stable in the sensitizers with 2-cyanoacrylic acid and cyanoacrylate as the anchor groups. On the other hand, our previous paper⁶³ has reported that sensitizer C258 with the cyanoacrylate as the anchor group can adsorb on TiO₂ anatase (101) surface in monodentate and bidentate bridging modes and the latter one is the most stable pattern. Although the other bidentate bridging mode has been observed where the chemisorption by two Ti–O bonds transfers to the Ti–N=C and Ti–O bonds and is stabilized by hydrogen-bond,^{80, 81} we only use the common bidentate bridging mode in this paper. Notably, for the discussion of aggregate pattern on substrate, we define the first monomer located in (0, 0) position is fragment F1 and the second monomer in another position is fragment F2 for simplification based on Fig. 2. Additionally, the oxygen atoms belong to cyanoacrylic acid in sensitizer and substrate are labeled as O_{S1/S2} and O_{Ti}, and the titanium atoms bond with O_{S1/S2} are distinguished as Ti_{1/2} (Fig. 5) to make a clear distinction of the followed analysis.

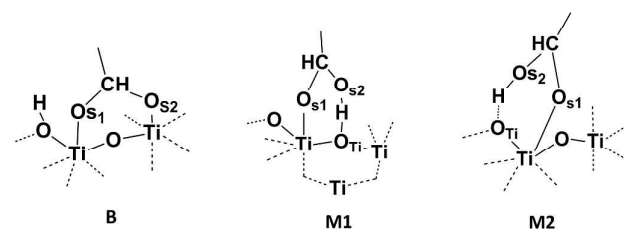


Fig. 5 The three main carboxylic/carboxylate adsorption modes in aggregate patterns of IQ4, YA421 and YA422.

Based on the structure of monomeric structure@substrate, the hydrogen of carboxylic acid in every sensitizer transfers to the adjacent oxygen on the substrate and the distances of Ti₁–O_{S1} and Ti₂–O_{S2} are ~ 2.02 to 2.10 Å (see Table S2 in Electronic Supplementary Information (ESI)). While for the dimeric structure, the different situations are found in YA421 and YA422 that the bidentate bridging in F1 and F2 become to the monodentate mode (M1 or M2) by H-bond of O_{S2}···H–O_{Ti} or O_{S2}–H···O_{Ti} (Fig. 5). However, this situation is unchanged in IQ4, which reveals by the distances of C–O_{S1}/C–O_{S2} (~ 1.28 to 1.30 Å) and Ti₁–O_{S1}/Ti₂–O_{S2} (~ 2.02 to 2.10 Å) are comparable to that of the monomeric structure on substrate (Table S2). In view of the conspicuous transformation of the adsorption mode, we will analyze the effect of extended donor subunit on the adsorption mode in YA421 and YA422 with respect to IQ4, and compared with the situation after the CDCA co-adsorbed.

3.2.1 Adsorption mode of aggregate YA421. For dimeric YA421, Fig. 6 (a)-(c) show the dynamical distances of H-bond, N···N atoms which both located in the donor group in F1 and F2 as well as the interaction between the two monomers as the function of the time span of 10 ps before and after the CDCA co-adsorption. Firstly, we analyzed the change tendency of H-bond in all dimeric structures. For (1, 1) pattern (Fig. 6 (a)), the H-bond of F1 and F2 (solid in black and pink) maintains a stable value ~ 0.90 to 1.00 Å before the CDCA co-adsorbed, while the obvious fluctuation after 2 ps is observed upon the CDCA presence (dot in pink). Moving to (0, 2) pattern (Fig. 6 (b)), the similar variation of H-bond is observed compared with (1, 1) pattern before the CDCA co-adsorption while the fluctuation presents after the CDCA co-adsorption. As for (2, 2) pattern, the up and down of H-bond is negligible in the simulated time range before and after the CDCA co-adsorption.

Subsequently, the averaged distances of N···N atoms are characterized to reflect the capacity of the anti-aggregation. For (1, 1) pattern (Fig. 6(a)), the variation of N···N distances is unobvious before and after CDCA co-adsorption (~ 5.57/5.47 Å, in gray and purple, respectively). While for (0, 2) pattern, this quantity is decreased from ~ 7.76 to 7.25 Å after co-adsorption with CDCA. Similarly, this value in (2, 2) pattern is also decreased after CDCA co-adsorption. This decreased N···N distances in the latter two patterns indicate that the adsorption with CDCA could contribute to stronger attraction between F1 and F2, then the parasitic lateral transfer of holes located in donor moiety⁸³ can lessen the efficiency of fast regeneration by redox media, consequently decreasing the J_{sc} .

Furthermore, the capacity of anti-aggregation can be characterized by the instantaneous intermolecular interaction between F1 and F2. For (1, 1) pattern, the interaction is comparable before and after the co-adsorption with CDCA (the average values are both around 2.99 eV, in blue and green, respectively). While for (0, 2) pattern, the average interaction is weakened from ~ 1.97 to 1.47 eV upon the CDCA co-adsorption. However, in (2, 2) pattern, this magnitude is slightly decreased ~ 0.04 eV after the co-adsorption with CDCA, indicating that the extended donor group possesses the capacity of anti-aggregation without the co-adsorption with CDCA. Meanwhile, the distances of H-bond and N···N show that the monomers F1 and F2 in (2, 2) pattern are more stable on the substrate before and after the CDCA co-adsorption with respect to (1, 1) and (0, 2) patterns. On the other hand, it could speculate that the transferred adsorption mode from bidentate bridging (monomeric structure) to monodentate (dimeric structure) is aroused from the van der Waals interaction via the two hexyloxy chains. Therefore, we deduce that the appropriate alignment of YA421 on the substrate is the (2, 2) pattern that it not only guarantees the compact adsorption but also prevents the π - π stacking.

3.2.2 Adsorption mode of aggregate YA422. In this section, the dynamics distances of H-bond, N···N between F1 and F2 as well as the interaction between the two monomers vs. 10 ps time span are discussed, and the corresponding data are

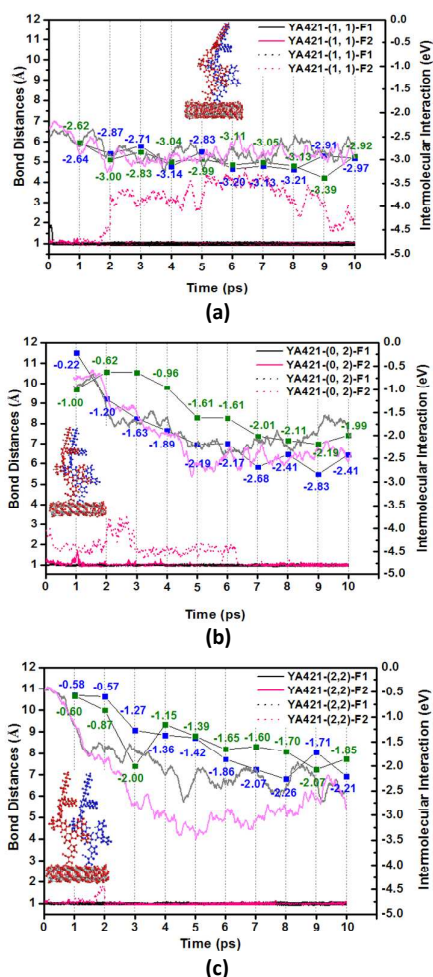


Fig. 6 The distances of H-bond and N \cdots N (both located in indoline group) and the intermolecular interaction energies (vs. the points-in-time) in series of aggregate pattern in YA421: (a) for (1, 1) (b) for (0, 2) and (c) for (2, 2) pattern, respectively (Solid and dot line in black and pink represent for H-bond in F1 (black) and F2 (pink) before and after CDCA co-adsorption. The line in gray and magenta stand for the distances of N \cdots N between F1 and F2 before and after CDCA co-adsorption, respectively. The interaction energies are marked in blue and green before and after CDCA co-adsorption, respectively).

summarized in Fig. 7 (a) and (b), respectively. For (0, 2) pattern (Fig. 7 (a)), the distances of H-bond is around 0.99 Å before the CDCA co-adsorption, but upon the CDCA presence, a small interference is detected from \sim 0.90 to 2.00 Å in the initial 2 ps and then maintains \sim 0.98 Å in the later 8 ps. However in (2, 2) pattern, this magnitude does not display an evident change in the whole time span before and after the co-adsorption with CDCA.

On the other hand, the N \cdots N distances in (0, 2) pattern tend to shorten from \sim 7.50 to 7.20 Å after the CDCA co-adsorption. Similarly, this value in (2, 2) pattern is also inclined to decrease from \sim 7.81 to 6.51 Å upon CDCA existence. Meanwhile, the average interaction between F1 and F2 in (0, 2) pattern is \sim 2.96 and \sim 3.00 eV before and after the CDCA co-adsorption. While in (2, 2) pattern, the quantity are both about 2.40 eV no matter how the CDCA co-adsorption. Based on the analysis

above, it is clearly that YA422 can prevent the aggregation, and this is evidenced by the negligible fluctuation of H-bond as well as the more separated donor part before CDCA co-adsorption. Moreover, the interaction also shows that the stable alignment can form in (0, 2) and (2, 2) patterns without the help of CDCA. In brief, the YA422 adsorbed on the substrate might be in the (2, 2) pattern as like as YA421 that the distances of H-bond and N \cdots N are comparable except the relative stronger interaction between F1 and F2, which is attributed to the Van der Waals interaction via more of the hexyloxy chains in YA422 can hamper the aggregation and ensure the denser alignment.

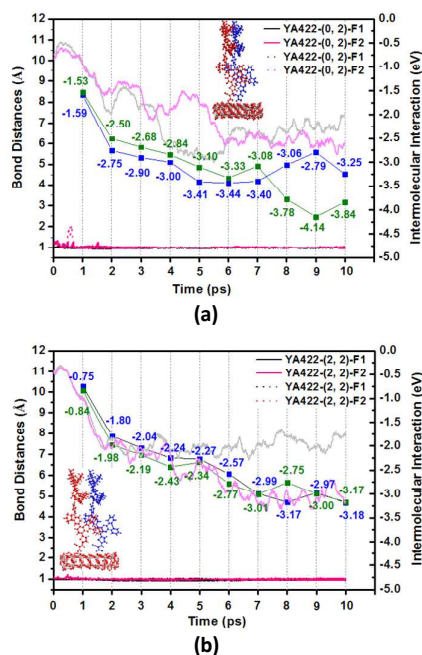


Fig. 7 The distances of H-bond and N \cdots N (both located in indoline group) and the intermolecular interaction energies (vs. the points-in-time) in series of aggregate pattern in YA422: (a) for (0, 2) and (b) for (2, 2) pattern, respectively (Solid and dot line in black and pink represent for H-bond in F1 (black) and F2 (pink) before and after CDCA co-adsorption. The line in gray and magenta stand for the distances of N \cdots N between F1 and F2 before and after CDCA co-adsorption, respectively. The interaction energies are marked in blue and green before and after CDCA co-adsorption, respectively).

3.3 Optical property of aggregate structures in sensitizers

As we know, the absorption of sensitizer on the substrate commonly presents a blue- or red-shift due to the H- or J-aggregation.^{84, 85} In view of the situation, the absorption of the aggregate structures on substrate has been simulated to further detect the influence of the extended donor part on the optical property. The calculated data is summarized in Table 3. Firstly, for IQ4, the maximum absorption λ_{\max} of all aggregate structures is blue-shifted and the oscillator strengths f are all strengthened compared to the monomeric structure (Table 1). Meanwhile, except the transition of λ_{\max} in (3, 1) pattern is originated from H \rightarrow L+1, the transition in other patterns is aroused from H \rightarrow L and this is distinguished from H \rightarrow L of monomeric IQ4. Table 3 also shows the transition isodensity plotting of these dimeric structures to distinguish the character

intuitively. It is noted that the transition from H→L+1 in (3, 1) structure featured with the intramolecular transition which is nearly localized on F1. While for (1, 1), (-1, 1) and (-3, 1) structures, the transition which related to H-1→L shows a combined intramolecular and intermolecular character. Thus the complete intramolecular transition only observed in (3, 1) structure indicates that the appropriate alignment can decrease the self-decay in the sensitizer monolayer and then enhance the electron injection.

As for the dimers of YA421, the λ_{\max} and f of all structures is red-shifted and strengthened with respect to the monomeric structure. Meanwhile, in (0, 2) and (2, 2) structures, the transition related to λ_{\max} is H-1→L+1, whereas in (1, 1) structure, the main contribution is triggered by H-1→L. The isodensity plotting for (1, 1) structure shows that the transition is the intermolecular charge transfer (ICT) from F1 to F2, whereas for (0, 2) and (2, 2) structures, the intramolecular CT from H-1→L+1 contributes to the transition. This picture of intramolecular CT in (0, 2) and (2, 2) structures is similar to IQ4-(3, 1) structure that the intramolecular CT is benefitted from the well separated F1 and F2.

Regarding the dimers of YA422, it is as similar as to the YA421 that the λ_{\max} of all dimeric structures is red-shifted and along with the enhanced intensity. At the same time, the λ_{\max} of (0, 2) structure is aroused from H-1→L+1 whereas attributed to H-3→L in (2, 2) structure, which these two transitions are both featured with a prominent intramolecular CT centered on F1. Based on the above analysis of transition properties, the blue-shift is by the order of IQ4, YA421 and YA422, simultaneously, the transition character is altered from the mixed inter- and intramolecular transition to the complete intramolecular CT from IQ4 to YA421 and YA422, which alleviates the self-quenching from the excited state to the ground state. The result elucidates the extended donor moiety can form the dense alignment of YA421 and YA422 on the substrate as well as guarantee a higher absorption and J_{sc} potentially.

3.4 Electronic coupling and electron injection rate

It is known that the photoinduced heterogeneous electron transfer is related by the electronic coupling between the sensitizer's LUMO orbital and the manifold virtue orbitals on TiO₂ substrate.^{70, 86} Therefore, to investigate the influence of the extended donor group on the mixing between the sensitizer's LUMO orbital and the conduction band of the substrate, the Lorentzian broadening $\rho_{LUMO}(E)$ and coupling strength of every sensitizer adsorbed on the substrate passing from IQ4 to YA422 have been modeled based on the Newns-Anderson approach. By using eqn (5), the obtained Lorentzian broadening is fitted in Fig. 8 (a)-(c), and the $E_{LUMO(ads)}$, the broadening width $\hbar\Gamma$ and the electron injection time τ are also obtained by using eqn (6)-(9), respectively. The results show that the mixing of LUMO orbital on sensitizer ($E_{LUMO(ads)}$) with the manifold unoccupied orbitals of TiO₂ are comparable in these three sensitizers (-2.99, -2.99 and -2.96 eV for IQ4, YA421 and YA422, respectively), simultaneously, a similar $\hbar\Gamma$ of 0.166 among these sensitizers are obtained. This little difference of

Table 3 Simulated absorption properties of the aggregate structure on substrate at MPW1K/6-31+G(d) level.

Aggregate structure	λ_{\max} nm/eV	transition character	f	isodensity ^a	
IQ4	(1,1)	522/2.37	H-1→L	1.83	
	(-1,1)	520/2.38	H-1→L	1.81	
	(3, 1)	523/2.37	H→L+1	1.87	
	(-3, 1)	522/2.37	H-1→L	1.43	
YA421	(1, 1)	579/2.14	H-1→L	1.85	
	(0, 2)	575/2.15	H-1→L+1	1.48	
	(2, 2)	577/2.15	H-1→L+1	1.59	
YA422	(0, 2)	580/2.14	H→L+1	1.57	
	(2, 2)	646/1.92	H-3→L	0.21	

^a The isodensity is related to the transition character

$E_{LUMO(ads)}$ among our considered cases is attributed to the subtle variation in molecular structure where only the donor group is extended. Meanwhile, the estimated electron-transfer time all fall in the femtosecond time range and have little

difference from IQ4 to YA422 (4.08, 3.96 and 3.96 fs, respectively).-

In view of the subtle difference in the electron-transfer time simulated by the Newns–Anderson approach above, the electron injection rate based on the Marcus equation has been evaluated to further explore the relationship between the extended donor unit and the outstanding efficiency for YA421 and YA422 with respect to IQ4. The required parameters to calculate the electron injection rate based on eqn (12)–(22) are collected in Table 4. Based on eqn (11), the smaller reorganization energy χ^{sen} and larger coupling constant V_{RP} and injection driving force ΔG_{inject} can achieve the faster injection rate k_{inject} . From Table 4, it is noted that the ΔG_{inject} in all sensitizers are comparable (the differences are ~ 0.02 to 0.04 eV), while the χ^{sen} and V_{RP} among these sensitizers are varied apparently. For IQ4, its larger χ^{sen} (0.69 eV) and the smaller V_{RP} (0.25 eV) can generate the relative lower k_{inject} of $0.74 \times 10^{15} \text{ s}^{-1}$. As for YA421, the estimated k_{inject} about $0.28 \times 10^{15} \text{ s}^{-1}$, the reason of this lower quantity is aroused from its largest χ^{sen} of 0.77 eV which unfavors the electron transfer although the higher V_{RP} of 0.40 eV is obtained. Contrarily, for YA422, although the relative smaller V_{RP} of 0.36 eV is calculated with respect to YA421, it still displays the largest k_{inject} by $2.27 \times 10^{15} \text{ s}^{-1}$, and this is benefited from its smaller χ^{sen} (0.59 eV) in all sensitizers, which can merit the electron transfer and the successive injection. The above results elucidate the extended donor group in YA422 can enhance the electron injection rate apparently and ensure the higher conversion efficiency compared to the other sensitizers based device.

3.5 Design of potential sensitizer

Based on the above analysis of intra-type FRET, we designed a new sensitizer DW1, where the donor D2' in YA422 is replaced by more extended moiety D3' (see Fig. 1) based on ref.43. The simulated absorption spectra of DW1 in comparison of IQ4 and YA422 are shown in Fig. 9. The obtained results show that the enhanced intra-FRET in DW1 is evidenced by near 3-folds higher in the absorption strength around 530 nm and an almost 1.26-folds faster k_{inject} ($2.87 \times 10^{15} \text{ s}^{-1}$) than that of YA422 ($2.27 \times 10^{15} \text{ s}^{-1}$). Thus, it is concluded that end-capped bulky size donor group properly can strength absorption and electron injection rate, and we speculate that this newly designed sensitizer DW1 could be a potential candidate for future high-efficiency DSSCs.

4. Conclusions

In this study, inspired by the prominent conversion efficiency of YA422-based solar cell, the DFT/TDDFT combined with the molecular dynamics simulation were performed to explore the relationship between the extended donor group and the higher efficiency compared with IQ4 and YA421-based cells. It is found that the intra-type FRET only occurs in YA422 where the energy transfers to the A- π -A backbone via luminescence of D2 subunit around the band of 533 nm and the absorption strength f_{abs} of this band is enhanced compared to IQ4 and YA421 with

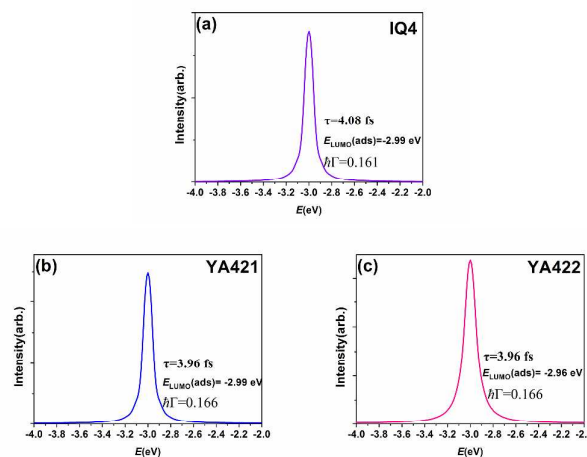


Fig. 8 Lorentzian broadening $\rho_{\text{LUMO}}(E)$ of (a) IQ4, (b) YA421 and (c) YA422. The corresponding fitting parameters $E_{\text{LUMO}}(\text{ads})$, broadening width $h\Gamma$ and lifetime τ are displayed.

Table 4 The parameters of χ (in eV), V_{RP} (in eV), ΔG_{inject} (in eV) and k_{inject} (in s^{-1}) in IQ4, YA421 and YA422.

Sensitizer	χ^{sen}	χ^{sol}	V_{RP}	ΔG_{inject}	k_{inject}
IQ4	0.69	0.09	0.25	-0.80	0.74×10^{15}
YA421	0.77	0.09	0.40	-0.74	0.28×10^{15}
YA422	0.59	0.08	0.36	-0.78	2.27×10^{15}

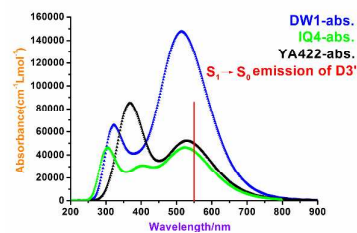


Fig. 9 Simulated absorption spectra in CH_2Cl_2 solution by MPW1K/6-31+G(d) level.

the smaller donor size. Meanwhile, the tendency of aggregation in YA422 is lessened compared with IQ4 and YA421 due to the steric hindrance introduced by the extended donor group, as a result, the self-decay in aggregate structure is weakened as evidenced by the transition character that the mixed intra- and intermolecular transition in IQ4 transfers to the complete intramolecular transition in YA422. Additionally, the combined Newns–Anderson approach and Marcus equation verify that the faster k_{inject} is achieved by YA422 compared to IQ4 and YA421. Our research provides fundamental insights on fact that the extension of donor part by a suitable electron's donating group can potentially enhance the conversion efficiency, and this has been applied to design potential candidate DW1 which possesses the donor D3' not only strengthens the absorption but also obtains larger electron injection rate.

Acknowledgements

This work is financially supported by the Major State Basic Research Development Programs of China (2011CBA00701), the National Natural Science Foundation of China (21473010, 21303007), and Beijing Key Laboratory for Chemical Power Source and Green Catalysis (2013CX02031). This work is also supported by the opening project of State Key Laboratory of Explosion Science and Technology (Beijing Institute of Technology) (ZDKT12-03).

References

- 1 M. Grätzel and B. O'Regan, *Nature*, 1991, **353**, 737–740.
- 2 L.-N. Yang, Z.-Z. Sun, Q.-S. Li, S.-L. Chen, Z.-S. Li and T. A. Niehaus, *J. Power Sources*, 2014, **268**, 137–145.
- 3 K. Kakiage, Y. Aoyama, T. Yano, K. Oya, T. Kyomen and M. Hanaya, *Chem. Commun.*, 2015, **51**, 6315–6317.
- 4 L.-N. Yang, S.-L. Chen and Z.-S. Li, *J. Mater. Chem. A*, 2015, **3**, 8308–8315.
- 5 G. Wang, Y. Wu, W. Ding, G. Yu, Z. Hu, H. Wang, S. Liu, Y. Zou and C. Pan, *J. Mater. Chem. A*, 2015, **3**, 14217–14227.
- 6 Z. Wu, X. Li, J. Li, H. Ågren, J. Hua and H. Tian, *J. Mater. Chem. A*, 2015, **3**, 14325–14333.
- 7 T. Lan, X. Lu, L. Zhang, Y. Chen, G. Zhou and Z.-S. Wang, *J. Mater. Chem. A*, 2015, **3**, 9869–9881.
- 8 Y. Hua, J. He, C. Zhang, C. Qin, L. Han, J. Zhao, T. Chen, W.-Y. Wong, W.-K. Wong and X. Zhu, *J. Mater. Chem. A*, 2015, **3**, 3103–3112.
- 9 Z.-Z. Sun, K.-M. Zheng, Q.-S. Li and Z.-S. Li, *RSC Adv.*, 2014, **4**, 31544.
- 10 M. Mba, M. D'Acunzo, P. Salice, T. Carofiglio, M. Maggini, S. Caramori, A. Campana, A. Aliprandi, R. Argazzi, S. Carli and C. A. Bignozzi, *J. Phys. Chem. C*, 2013, **117**, 19885–19896.
- 11 C. Li, S.-J. Wu and C.-G. Wu, *J. Mater. Chem. A*, 2014, **2**, 17551–17560.
- 12 L. D'Amario, G. Boschloo, A. Hagfeldt and L. Hammarström, *J. Phys. Chem. C*, 2014, **118**, 19556–19564.
- 13 S. Pan, X. Liu, M. Guo, S. f. Yu, H. Huang, H. Fan and G. Li, *J. Mater. Chem. A*, 2015, **3**, 11437–11443.
- 14 Y. Duan, J. Zheng, M. Xu, X. Song, N. Fu, Y. Fang, X. Zhou, Y. Lin and F. Pan, *J. Mater. Chem. A*, 2015, **3**, 5692–5700.
- 15 M. J. Ju, J. C. Kim, H.-J. Choi, I. T. Choi, S. G. Kim, K. Lim, J. Ko, J.-J. Lee, I.-Y. Jeon, J.-B. Baek and H. K. Kim, *ACS Nano*, 2013, **7**, 5243–5250.
- 16 J. Ma, W. Shen, C. Li and F. Yu, *J. Mater. Chem. A*, 2015, **3**, 12307–12313.
- 17 T. Etienne, L. Chbib, C. Michaux, E. A. Perpète, X. Assfeld and A. Monari, *Dyes Pigm.*, 2014, **101**, 203–211.
- 18 Y. Numata, A. Islam, H. Chen and L. Han, *Energy Environ. Sci.*, 2012, **5**, 8548.
- 19 C.-P. Hsu, *Acc. Chem. Res.*, 2009, **42**, 509–518.
- 20 H. Ma and A. Troisi, *J. Phys. Chem. C*, 2014, **118**, 27272–27280.
- 21 M. Pastore and F. De Angelis, *ACS Nano*, 2010, **4**, 556–562.
- 22 K. Pei, Y. Wu, H. Li, Z. Geng, H. Tian and W.-H. Zhu, *ACS Appl. Mater. Interfaces*, 2015, **7**, 5296–5304.
- 23 H. Kusama, T. Funaki, N. Koumura and K. Sayama, *Phys. Chem. Chem. Phys.*, 2014, **16**, 16166–16175.
- 24 C.-L. Lin and C.-M. Chu, *Energy Procedia*, 2014, **61**, 842–845.
- 25 Y. Hua, L. T. Lin Lee, C. Zhang, J. Zhao, T. Chen, W.-Y. Wong, W.-K. Wong and X. Zhu, *J. Mater. Chem. A*, 2015, **3**, 13848–13855.
- 26 H. Zhu, Y. Wu, J. Liu, W. Zhang, W. Wu and W.-H. Zhu, *J. Mater. Chem. A*, 2015, **3**, 10603–10609.
- 27 C. Lelii, M. G. Bawendi, P. Biagini, P.-Y. Chen, M. Crucianelli, J. M. D'Arcy, F. De Angelis, P. T. Hammond and R. Po, *J. Mater. Chem. A*, 2014, **2**, 18375–18382.
- 28 X. Sun, Y. Wang, X. Li, H. Ågren, W. Zhu, H. Tian and Y. Xie, *Chem. Commun.*, 2014, **50**, 15609–15612.
- 29 X. Lu, T. Lan, Z. Qin, Z.-S. Wang and G. Zhou, *ACS Appl. Mater. Interfaces*, 2014, **6**, 19308–19317.
- 30 P. Salvatori, G. Marotta, A. Cinti, C. Anselmi, E. Mosconi and F. De Angelis, *J. Phys. Chem. C*, 2013, **117**, 3874–3887.
- 31 Y. Wei, Z. Wu, Z. An, X. Chen, P. Chen and Q. Liu, *Chin. J. Chem.*, 2014, **32**, 474–478.
- 32 J. I. Basham, G. K. Mor and C. A. Grimes, *ACS Nano*, 2010, **4**, 1253–1258.
- 33 M. D. Brown, P. Parkinson, T. Torres, H. Miura, L. M. Herz and H. J. Snaith, *J. Phys. Chem. C*, 2011, **115**, 23204–23208.
- 34 B. E. Hardin, E. T. Hoke, P. B. Armstrong, J.-H. Yum, P. Comte, T. Torres, J. M. J. Fréchet, M. K. Nazeeruddin, M. Grätzel and M. D. McGehee, *Nat. Photonics*, 2009, **3**, 406–411.
- 35 B. E. Hardin, J. H. Yum, E. T. Hoke, Y. C. Jun, P. Pechy, T. Torres, M. L. Brongersma, M. K. Nazeeruddin, M. Grätzel and M. D. McGehee, *Nano. Lett.*, 2010, **10**, 3077–3083.
- 36 G. K. Mor, J. Basham, M. Paulose, S. Kim, O. K. Varghese, A. Vaish, S. Yoriya and C. A. Grimes, *Nano. Lett.*, 2010, **10**, 2387–2394.
- 37 J.-H. Yum, B. E. Hardin, S.-J. Moon, E. Baranoff, F. Nuesch, M. D. McGehee, M. Grätzel and M. K. Nazeeruddin, *Angew. Chem. Int. Ed.*, 2009, **48**, 9277–9280.
- 38 H. J. Yun, D. Y. Jung, D. K. Lee, A. K.-Y. Jen and J. H. Kim, *Dyes Pigm.*, 2015, **113**, 675–681.
- 39 R. Y.-Y. Lin, Y.-S. Yen, Y.-T. Cheng, C.-P. Lee, Y.-C. Hsu, H.-H. Chou, C.-Y. Hsu, Y.-C. Chen, J. T. Lin, K.-C. Ho and C. Tsai, *Org. Lett.*, 2012, **14**, 3612–3615.
- 40 Y. Wang, B. Chen, W. Wu, X. Li, W. Zhu, H. Tian and Y. Xie, *Angew. Chem. Int. Ed.*, 2014, **53**, 10779–10783.
- 41 V. Dryza and E. J. Bieske, *J. Phys. Chem. C*, 2014, **118**, 19646–19654.
- 42 G. Marotta, M. A. Reddy, S. P. Singh, A. Islam, L. Han, F. De Angelis, M. Pastore and M. Chandrasekharan, *ACS Appl. Mater. Interfaces*, 2013, **5**, 9635–9647.
- 43 H. Choi, N. Cho, S. Paek and J. Ko, *J. Phys. Chem. C*, 2014, **118**, 16319–16327.
- 44 J. Yang, P. Ganesan, J. Teuscher, T. Moehl, Y. J. Kim, C. Yi, P. Comte, K. Pei, T. W. Holcombe, M. K. Nazeeruddin, J. Hua, S. M. Zakeeruddin, H. Tian and M. Grätzel, *J. Am. Chem. Soc.*, 2014, **136**, 5722–5730.

- 45 L. Wang, M. Liang, Y. Zhang, F. Cheng, X. Wang, Z. Sun and S. Xue, *Dyes Pigm.*, 2014, **101**, 270-279.
- 46 H. Zhu, W. Li, Y. Wu, B. Liu, S. Zhu, X. Li, H. Ågren and W. Zhu, *ACS Sustain. Chem. Eng.*, 2014, **2**, 1026-1034.
- 47 D. Kuang, S. Uchida, R. Humphry-Baker, S. M. Zakeeruddin and M. Grätzel, *Angew. Chem. Int. Ed.*, 2008, **47**, 1923-1927.
- 48 Y. Wu, X. Zhang, W. Li, Z.-S. Wang, H. Tian and W. Zhu, *Adv. Energ. Mater.*, 2012, **2**, 149-156.
- 49 W. Zhu, Y. Wu, S. Wang, W. Li, X. Li, J. Chen, Z.-S. Wang and H. Tian, *Adv. Funct. Mater.*, 2011, **21**, 756-763.
- 50 G. Li, M. Liang, H. Wang, Z. Sun, L. Wang, Z. Wang and S. Xue, *Chem. Mater.*, 2013, **25**, 1713-1722.
- 51 K. Pei, Y. Wu, A. Islam, S. Zhu, L. Han, Z. Geng and W. Zhu, *J. Phys. Chem. C*, 2014, **118**, 16552-16561.
- 52 Y. Wu, W. H. Zhu, S. M. Zakeeruddin and M. Grätzel, *ACS Appl. Mater. Interfaces*, 2015, **7**, 9307-9318.
- 53 S. Ito, H. Miura, S. Uchida, M. Takata, K. Sumioka, P. Liska, P. Comte, P. Péchy and M. Grätzel, *Chem. Commun.*, 2008, 5194-5196.
- 54 K. Pei, Y. Wu, A. Islam, Q. Zhang, L. Han, H. Tian and W. Zhu, *ACS Appl. Mater. Interfaces*, 2013, **5**, 4986-4995.
- 55 K. Raghavachari, *Theor. Chem. Acc.*, 2000, **103**, 361-363.
- 56 A. D. Becke, *J. Chem. Phys.*, 1993, **98**, 1372-1377.
- 57 B.-Q. Yao, J.-S. Sun, Z.-F. Tian, X.-M. Ren, D.-W. Gu, L.-J. Shen and J. Xie, *Polyhedron*, 2008, **27**, 2833-2844.
- 58 S. Grimme, *Wiley. Interdiscip. Rev. Comput. Mol. Sci.*, 2011, **1**, 211-228.
- 59 M. Cossi, N. Rega, G. Scalmani and V. Barone, *J. Comput. Chem.*, 2003, **24**, 669-681.
- 60 M. J. Frisch, G. W. Trucks, H. B. Schlegel, G. E. Scuseria, M. A. Robb, J. R. Cheeseman, G. Scalmani, V. Barone, B. Mennucci, G. A. Petersson, H. Nakatsuji, M. Caricato, X. Li, H. P. Hratchian, A. F. Izmaylov, J. Bloino, G. Zheng, J. L. Sonnenberg, M. Hada, M. Ehara, K. Toyota, R. Fukuda, J. Hasegawa, M. Ishida, T. Nakajima, Y. Honda, O. Kitao, H. Nakai, T. Vreven, J. A. Montgomery, J. E. Peralta Jr., F. Ogliaro, M. Bearpark, J. J. Heyd, E. Brothers, K. N. Kudin, V. N. Staroverov, R. Kobayashi, J. Normand, K. Raghavachari, A. Rendell, J. C. Burant, S. S. Iyengar, J. Tomasi, M. Cossi, N. Rega, J. M. Millam, M. Klene, J. E. Knox, J. B. Cross, V. Bakken, C. Adamo, J. Jaramillo, R. Gomperts, R. E. Stratmann, O. Yazyev, A. J. Austin, R. Cammi, C. Pomelli, J. W. Ochterski, R. L. Martin, K. Morokuma, V. G. Zakrzewski, G. A. Voth, P. Salvador, J. J. Dannenberg, S. Dapprich, A. D. Daniels, O. Farkas, J. B. Foresman, J. V. Ortiz, J. Cioslowski and D. J. Fox, Gaussian 09, Revision D.01, Wallingford CT, Gaussian Inc., 2009.
- 61 B. Aradi, B. Hourahine and T. Frauenheim, *J. Phys. Chem. A*, 2007, **111**, 5678-5684.
- 62 Aradi, B. and Hourahine, B, DFTB+ Version 1.2, Density Functional Based Tight Binding, Available at <http://www.DFTB-Plus.info>.
- 63 P.-P. Sun, Q.-S. Li, L.-N. Yang, Z.-Z. Sun and Z.-S. Li, *Phys. Chem. Chem. Phys.*, 2014, **16**, 21827-21837.
- 64 S. Feng, Q.-S. Li, L.-N. Yang, Z.-Z. Sun, T. A. Niehaus and Z.-S. Li, *J. Power Sources*, 2015, **273**, 282-289.
- 65 W. Fan, D. Tan and W.-Q. Deng, *Chemphyschem.*, 2012, **13**, 2051-2060.
- 66 C. F. A. Negre, V. C. Fuertes, M. B. Oviedo, F. Y. Oliva and C. G. Sánchez, *J. Phys. Chem. C*, 2012, **116**, 14748-14753.
- 67 M. Pastore and F. De Angelis, *J. Phys. Chem. Lett.*, 2012, **3**, 2146-2153.
- 68 H. Wang, B. Yue, Z. Xie, B. Gao, Y. Xu, L. Liu, H. Sun and Y. Ma, *Phys. Chem. Chem. Phys.*, 2013, **15**, 3527-3534.
- 69 J. P. Muscat and D. M. Newns, *Prog. Surf. Sci.*, 1978, **9**, 1-43.
- 70 P. Persson, M. J. Lundqvist, R. Ernstorfer, W. A. Goddard and F. Willig, *J. Chem. Theory. Comput.*, 2006, **2**, 441-451.
- 71 J. Calbo, M. Pastore, E. Mosconi, E. Orti and F. De Angelis, *Phys. Chem. Chem. Phys.*, 2014, **16**, 4709-4719.
- 72 C. Dong, X. Li, W. Zhao, P. Jin and J. Qi, *J. Phys. Chem. C*, 2013, **117**, 9092-9103.
- 73 J. Preat, *J. Phys. Chem. C*, 2010, **114**, 16716-16725.
- 74 K. L. Syres, A. G. Thomas, W. R. Flavell, B. F. Spencer, F. Bondino, M. Malvestuto, A. Preobrajenski and M. Grätzel, *J. Phys. Chem. C*, 2012, **116**, 23515-23525.
- 75 B. Kim, S. W. Park, J.-Y. Kim, K. Yoo, J. A. Lee, M.-W. Lee, D.-K. Lee, J. Y. Kim, B. Kim, H. Kim, S. Han, H. J. Son and M. J. Ko, *ACS Appl. Mater. Interfaces*, 2013, **5**, 5201-5207.
- 76 F. Zhang, F. Shi, W. Ma, F. Gao, Y. Jiao, H. Li, J. Wang, X. Shan, X. Lu and S. Meng, *J. Phys. Chem. C*, 2013, **117**, 14659-14666.
- 77 A. Akbari, J. Hashemi, J. Niskanen, S. Huotari and M. Hakala, *Phys. Chem. Chem. Phys.*, 2015, **17**, 10849-10855.
- 78 W. Li, L. G. C. Rego, F.-Q. Bai, J. Wang, R. Jia, L.-M. Xie and H.-X. Zhang, *J. Phys. Chem. Lett.*, 2014, **5**, 3992-3999.
- 79 N. Martsinovich, D. R. Jones and A. Troisi, *J. Phys. Chem. C*, 2010, **114**, 22659-22670.
- 80 F. Zhang, W. Ma, Y. Jiao, J. Wang, X. Shan, H. Li, X. Lu and S. Meng, *ACS Appl. Mater. Interfaces*, 2014, **6**, 22359-22369.
- 81 W. Ma, Y. Jiao and S. Meng, *Phys. Chem. Chem. Phys.*, 2013, **15**, 17187-17194.
- 82 M. Pastore and F. De Angelis, *J. Phys. Chem. Lett.*, 2013, **4**, 956-974.
- 83 V. Vaissier, E. Mosconi, D. Moia, M. Pastore, J. M. Frost, F. De Angelis, P. R. F. Barnes and J. Nelson, *Chem. Mater.*, 2014, **26**, 4731-4740.
- 84 Y. Wang, T. Liu, L. Bu, J. Li, C. Yang, X. Li, Y. Tao and W. Yang, *J. Phys. Chem. C*, 2012, **116**, 15576-15583.
- 85 S. Yagai, T. Seki, T. Karatsu, A. Kitamura and F. Würthner, *Angew. Chem. Int. Ed.*, 2008, **47**, 3367-3371.
- 86 K. S. V. Gupta, J. Zhang, G. Marotta, M. A. Reddy, S. P. Singh, A. Islam, L. Han, F. De Angelis, M. Chandrasekharan and M. Pastore, *Dyes Pigm.*, 2015, **113**, 536-545.